

Attosecond electron dynamics: A multiresolution approach

Nicholas Vence,¹ Robert Harrison,^{2,3} and Predrag Krstić^{1,3,*}

¹*Department of Physics and Astronomy, University of Tennessee, Knoxville, Tennessee 37996, USA*

²*Department of Chemistry, University of Tennessee, Knoxville, Tennessee 37996, USA*

³*Oak Ridge National Laboratory, Oak Ridge, Tennessee 37831, USA*

(Received 6 July 2011; revised manuscript received 31 October 2011; published 2 March 2012)

We establish a numerical solution to the time-dependent Schrödinger equation employing an adaptive, discontinuous spectral element basis that automatically adjusts to the requested precision. The explicit time evolution is accomplished by a band-limited, gradient-corrected, symplectic propagator and uses separated representations of operators for efficient computation in multiple dimensions. We illustrate the method calculating accurate bound and continuum transition probabilities along with the photoelectron spectra for $H(1s)$, $He^+(1s)$, and $Li^{2+}(2s)$ in three dimensions and H_2^+ in three and four dimensions under a two-cycle attosecond laser pulse with driving frequency of 36 eV and an intensity of 1×10^{15} W/cm².

DOI: [10.1103/PhysRevA.85.033403](https://doi.org/10.1103/PhysRevA.85.033403)

PACS number(s): 32.80.Rm, 31.15.ac, 32.80.Fb

I. INTRODUCTION

Collisions of electrons, ions, and photons with molecules and atoms create energetic species that drive chemical and physical changes in environments ranging from plasmas to living tissue; predicting these changes requires an understanding of the fundamental underlying processes. This article details the development of an effective time-evolution scheme and establishes its accuracy through three-dimensional (3D) benchmark studies of the one-electron species H , He^+ , and Li^{2+} in a two-cycle attosecond laser pulse by presenting bound and continuum transition probabilities along with photoelectron spectra. Single-electron dynamics has served to debut many established methods [1–13]. We extend a highly accurate method of computational chemistry [14–17] toward a robust description of many-electron systems, beyond the single-electron approximation. As H_2^+ is taken from 3D to 4D we add multiresolution analysis [18–20] to the rapidly growing body of research in dynamic nuclear-electron coupling [21–28].

The standard *ab initio*, few-electron solutions to the time-dependent Schrödinger equation (TDSE) [29–42] for electron-photon scattering are time-dependent grid methods and time-independent close-coupling-type approaches with a large number of physical and pseudo states. While great progress has been made in chemistry modeling complex molecules and clusters close to their electronic ground state, the inclusion of the highly excited bound and continuum states has been the crucial challenge in many-electron transition dynamics. The simplicity of our method comes from a unified treatment of the bound and continuum states and the high level of programming abstraction using operators and functions whose mesh automatically adapts to guarantee the requested precision. It does not rely on special coordinates or symmetry to treat singularities or reduce the dimensionality. Currently it can accommodate an elliptically polarized laser pulse and is readily extendable to describe the dynamics of a multiparticle system using either the standard multiconfiguration wave

function or a fully correlated, many-dimension, few-particle wave function of electrons and/or nuclei.

We are numerically solving the TDSE of a finite laser pulse in the length gauge within the dipole approximation (atomic units are used throughout the text, unless stated otherwise)

$$i \frac{d\Psi}{dt} = \hat{H} \Psi \quad \hat{H} = -\frac{1}{2} \nabla^2 + V(r) + \mathbf{E}(t) \cdot \mathbf{r}, \quad (1)$$

where $\mathbf{E}(t)$ is the electric field strength and $V(r)$ is the atomic potential. The n_{cy} cycle pulse of duration T ,

$$\begin{aligned} \mathbf{E}(t) &= E_0 \sin^2(\omega t / 2n_{cy}) \cos(\omega t + \varphi) \hat{\mathbf{z}} \\ 0 \leq t &< \frac{2\pi n_{cy}}{\omega} = T, \end{aligned} \quad (2)$$

has a carrier envelope phase of $\varphi = -\pi/2$. These parameters were chosen to match the isolated attosecond pulse [43] crafted by Sansone *et al.* This linearly polarized, two-cycle, ultraviolet laser pulse has a central photon energy of $\omega = 1.32$ (36 eV), peak intensity $I = 10^{15}$ W/cm², i.e., $E_0 = 0.176$, and duration 9.6 (230 as). The power spectrum of the two-cycle pulse (see Fig. 1) spans many bound and continuum states and can be thought of as a multimode laser with a continuum of frequencies.

MADNESS (Multiresolution ADaptive Numerical Environment for Scientific Simulation) [15–17,44] provides a front end for scientists who wish to apply the multiresolution framework [14] without focusing on the low-level math or the computational implementation. It is an interface to functions and operators that keeps track of the numerical precision, the hardware optimization, and the message-passing interface of modern, distributed-memory computers. In MADNESS functions are represented on an N-dimensional mesh where each subdomain contains a tensor product of Legendre polynomials that adapts to meet the precision requirements. Our multiresolution approach is based upon the principles outlined by Alpert *et al.* [14], while Fann *et al.* [17] give a comprehensive introduction of MADNESS to the computational science community.

In Sec. II, we explore the spatial and temporal discretizations as expressed in the multiresolution framework. Since the linearly polarized pulses impose azimuthal symmetry on

*krsticp@ornl.gov

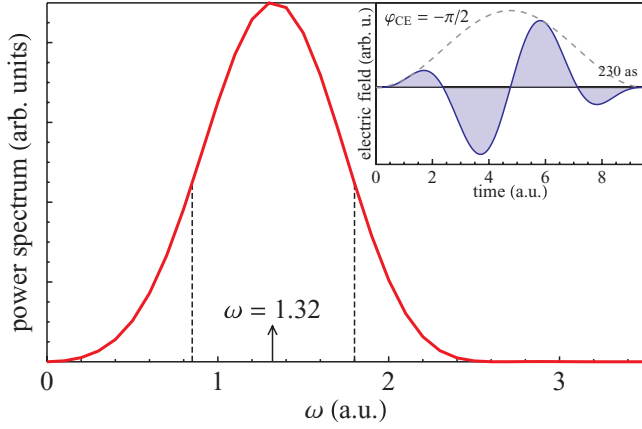


FIG. 1. (Color online) The linearly polarized, two-cycle laser pulse with a driving frequency of 36 eV, intensity of 1×10^{15} W/cm², and a carrier envelope phase of $-\pi/2$ chosen to match that of Sansone *et al.* [43].

a spherically symmetric system, we assume the azimuthal quantum number $m = 0$ throughout this paper. While a 2D simulation would have described the system completely, the 3D representation allows extension to systems without cylindrical symmetry and will provide a useful reference point for future work. Section III describes the projection onto the continuum, numerical convergence, comparison with an established *ab initio* scheme, and other issues pertaining to the 3D implementation. We discuss the highlights of this pulse acting on H(1s), He⁺(1s), and Li²⁺(2s) along with H₂⁺ in Sec. IV.

II. THEORY

A. Spatial representation

Multiresolution analysis within a multiwavelet basis [14] is best explored with a 1D function f . At the coarsest level ($n = 0$), f is represented by a linear combination of scaling functions

$$\phi_i(x) = \begin{cases} \sqrt{2i+1} P_i(2x-1) & x \in [0, 1] \\ 0 & \text{otherwise,} \end{cases} \quad (3)$$

where $P_i(x)$ are the Legendre polynomials. These parent scaling functions ($n = 0$) are shifted and dilated as f is refined. The first level of refinement ($n = 1$) splits the domain and represents each side with an independent set of k scaling functions:

$$\phi_{i\ell}^n(x) = 2^{n/2} \phi_i(2^n x - \ell). \quad (4)$$

At level n of refinement there are 2^n subdomains that are indexed by ℓ .

In MADNESS, each subdomain of f is adaptively refined until it satisfies the requested numerical tolerance ϵ . f is represented (see Fig. 2) by subdomains (boxes) that cover the original domain:

$$f^{(\epsilon)}(x) = \sum_{n\ell} \sum_{i=0}^{k-1} s_{i\ell}^n \phi_{i\ell}^n(x), \quad s_{i\ell}^n = \int f(x) \phi_{i\ell}^n(x) dx. \quad (5)$$

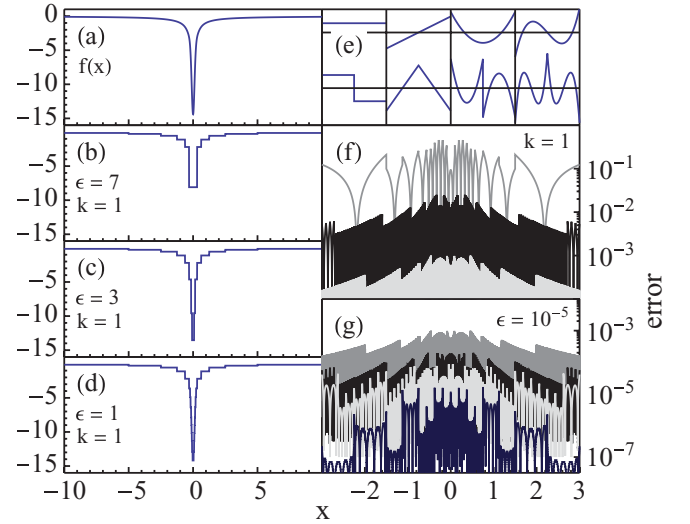


FIG. 2. (Color online) The function $f(x)$ in (a) is approximated in (b)–(d) showing refinement (at $k = 1$) with successively smaller numerical thresholds ϵ . In (e) the first four scaling functions [from Eq. (5)] are shown above their corresponding wavelets [from Eq. (7)]. The absolute value of the refinement error is shown in (f) with $k = 1$ and $\epsilon = 10^{-1}, 10^{-3}, 10^{-5}$; and in (g) with $\epsilon = 10^{-5}$ and $k = 1, 2, 3, 6$.

Each scaling function $\phi_{i\ell}^n(x)$ [see Fig. 2(e) upper row] has a corresponding wavelet function $\psi_{i\ell}^n(x)$ [see Fig. 2(e) lower row]:

$$\psi_{i\ell}^n(x) = \phi_{i2\ell}^{n+1}(x) - \phi_{i2\ell+1}^{n+1}(x). \quad (6)$$

This provides a second mathematically equivalent representation of f :

$$f^{(\epsilon)}(x) = \sum_{i=0}^{k-1} s_{i\ell}^0 \phi_{i\ell}^0(x) + \sum_{n\ell} \sum_{i=0}^{\text{boxes } k-1} d_{i\ell}^n \psi_{i\ell}^n(x), \quad (7)$$

$$d_{i\ell}^n = \int f(x) \psi_{i\ell}^n(x) dx.$$

The wavelets provide a more efficient basis for certain operations due to the following orthogonality relations:

$$\begin{aligned} \int \phi_{i\ell}^n(x) \phi_{i'\ell'}^{n'}(x) dx &= \delta_{nn'} \delta_{\ell\ell'} \delta_{ii'}, \\ \int \psi_{i\ell}^n(x) \psi_{i'\ell'}^{n'}(x) dx &= \delta_{nn'} \delta_{\ell\ell'} \delta_{ii'}, \\ \int \phi_{i\ell}^n(x) \psi_{i'\ell'}^{n'}(x) dx &= 0 \quad \text{if } n > n'. \end{aligned} \quad (8)$$

There exists a fast transform between the scaling function representation in Eq. (5) and wavelet representation in Eq. (7). This dual representation is analogous to the coordinate-momentum representation.

Function refinement, the recursive subdivision of the domain, continues until the difference coefficients satisfy the refinement criteria;

$$\|d_\ell^n\|_2 = \sqrt{\sum_i |d_{i\ell}^n|^2} \leq \epsilon. \quad (9)$$

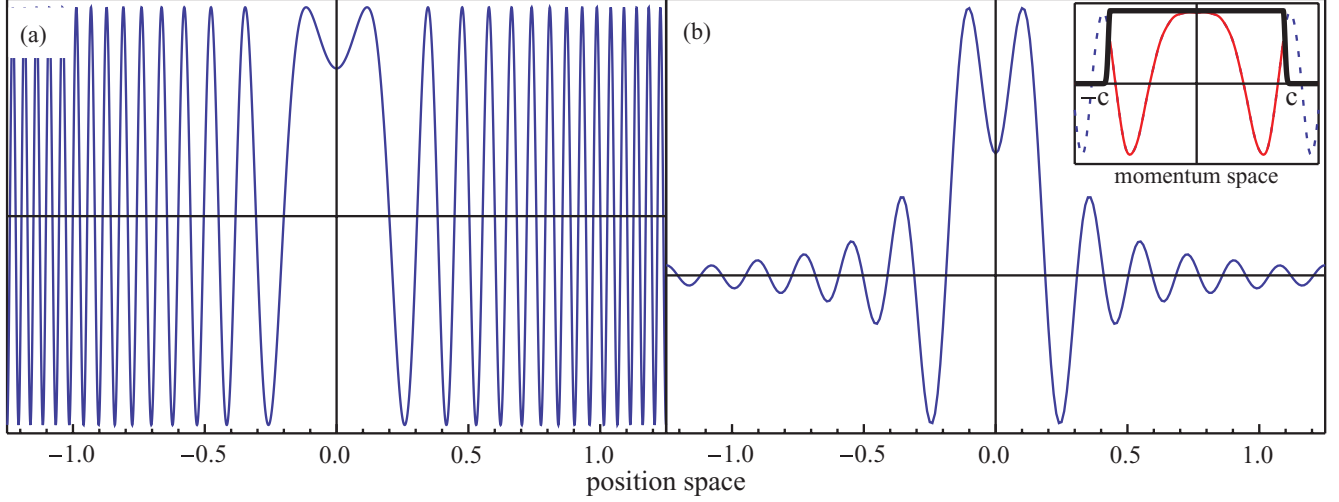


FIG. 3. (Color online) (a) The real component of the 1D free particle propagator and (b) its band-limited counterpart. The band-limit (inset in momentum space) is the black line and the excluded Fourier components of the original function are dashed.

The refinement is deepest in regions where f is not smooth (see Fig. 2). The approximation error for a locally smooth function scales as $O(2^{-nk})$, while the error near a discontinuity scales as $O(2^{-n})$. A typical, low-accuracy run of the TDSE for the hydrogen atom ($k = 12$, $\epsilon = 1 \times 10^{-5}$, and $\xi = 0.3$) (see Sec. II C) refines to a depth of $n = 9$ while a high-precision run ($\xi = 0.05$, $k = 24$, and $\epsilon = 1 \times 10^{-7}$) refines to $n = 11$.

The Cartesian coordinate representation, while not necessary for simulation in MADNESS, carries many benefits. It is easy to extend a function to an arbitrary number of spatial dimensions while maintaining a consistent interface with the operators. Thus, the implementation of the 3D solution to the TDSE is only marginally more complicated than that of a 1D solution, and the extension of 3D atomic hydrogen to fixed nuclear H_2^+ was only a modification of the input file parameters. In Sec. IV D we provide preliminary results from a 4D representation of H_2^+ where the internuclear separation is treated dynamically, on the same footing as the 3D electronic components. A 6D treatment of two-electron He, while more computationally intensive, requires only the addition of an electron-electron repulsion term to the Hamiltonian.

In summary, the multiresolution formalism provides the impression of a basis-free simulation by automating the extension or contraction of the basis through adaptive refinement. Most *ab initio* schemes compute matrix elements to machine precision within a fixed, finite basis. MADNESS, however, computes to finite precision in a dynamically changing basis. Finally, the Cartesian framework of MADNESS is readily extendable to larger systems.

B. Time evolution

For the temporal propagation of the TDSE [Eq. (1)], we employ the fourth-order, gradient-corrected, symplectic propagator developed by Chin and Chen [45]. This time evolution operator,

$$\begin{aligned} \mathcal{U}(dt, t) = & e^{-i\frac{1}{6}V(t+dt)dt} e^{-i\frac{1}{2}\hat{T}dt} e^{-i\frac{2}{3}V(t+\frac{1}{2}dt)dt} \\ & \times e^{-i\frac{1}{2}\hat{T}dt} e^{-i\frac{1}{6}V(t)dt} + O(dt^5), \end{aligned} \quad (10)$$

reduces the error and total computational expense by allowing a much longer time steps than the second-order accurate, Trotter splitting [46]. The application of the exponentiated potential in MADNESS is simply function multiplication, while the application of the exponentiated kinetic energy operator

$$\mathcal{U}_0(t) = e^{-i\frac{1}{2}\hat{T}dt} = e^{i\nabla^2 dt/4} \quad (11)$$

is an integral convolution. The potential-free Green's function (free-particle propagator) of the TDSE in D spatial dimensions

$$G_0(x, t) = (2\pi i dt)^{-D/2} e^{-\frac{x^2}{2dt}} \quad (12)$$

is applied to the wave function

$$\begin{aligned} \psi(x, dt) &= \mathcal{U}_0(dt) \psi(x, 0) \\ &= \int dx' G_0(x - x', dt) \psi(x', 0), \end{aligned} \quad (13)$$

advancing it forward in time.

The unbounded spectrum of the kinetic energy operator \mathcal{U}_0 in Fig. 3(a) makes its complete computational representation impossible. However, we are not interested in representing the full operator, only the components necessary for the propagation of a band-limited wave function. This is directly analogous to the upper energy limit on a uniform grid. The band-limit is applied by transforming the full G_0 to momentum space [see inset in Fig. 3(b)], multiplying by a band-limiting filter, and transforming back to real space [Fig. 3(b)]. The band-limited G_0 is compact both in position space and momentum space.

The discontinuous, spectral element basis is a computationally convenient alternative to the finite-element or finite-difference methods. Continuity emerges (within finite precision) with the application of an appropriately constructed integral or differential operator [14], as is the case with the stencils used in finite-difference methods. Nevertheless, the adaptive, discontinuous, polynomial basis unavoidably includes numerical, high-frequency components, even when representing smooth functions. The insensitivity of the

band-limited G_0 to this numerical noise preserves the integrity of the wave function.

Scattering off the Coulomb singularity also allows arbitrarily high frequencies into the wave function. These legitimate physical frequencies would introduce propagation error upon application of the band-limited G_0 . We prevent this error by band-limiting the nuclear potential (see Sec. II C) to allow exact propagation. This is accomplished by smoothing the singularity at a closest scattering distance, which prevents high frequencies from entering the system. The cutoff parameter ξ controls the depth of the potential, the band-limit, and the complexity of the simulation (see Sec. III B 3).

In addition to increasing the size of the wave function, the fine spatial variations associated with high frequencies require an impractically small time step. The TDSE is limited by a Courant-Friedrichs-Lewy-like [47] condition ($dt \propto \Delta x^2$) with the critical time step

$$dt_{\text{crit}} \simeq 2\pi/c^2 \propto (\Delta x)^2 \propto \xi^2, \quad (14)$$

where c is an empirically estimated band-limit and Δx is the smallest mesh spacing that is controlled by ξ , the potential smoothing parameter.

The application of G_0 (from Fig. 3) is the most computationally intensive step of time evolution and efficiency hinges on its separability. While computer memory limits the size of the solution domain in fixed grid schemes, in MADNESS, memory limits the total complexity of the wave function. Massively parallel, distributed-memory computers replace the memory constraint by a communication bandwidth limit. For a sufficiently large number of computational nodes, the convolution of G_0 is bottlenecked by interprocessor communication. The application cost of a general D -dimensional convolution of a wave function with N coefficients scales as $O(N^{2D})$. A 3D convolution $G_0(x, y, z, x', y', z') * \psi(x, y, z)$ requires six spatial indices. MADNESS takes advantage of the separable nature of the Gaussian form of G_0 [see Eq. (12)] to accomplish the time evolution of a higher dimension system by repeated application of the 1D propagator:

$$\prod_i G_0(x_i, x'_i) * \psi(x, y, z) \quad x_i \in (x, y, z), \quad (15)$$

which scales as $O(N^{D+1})$. The reduced data transfer enables the time evolution of higher dimension systems. Details concerning the choice of the frequency windowing function, parametrization of the effective band-limit, and accurate application of this oscillatory operator are found in the MADNESS implementation notes [44].

In summary, successful time evolution of a multiresolution wave function hinges on the band-limit. First, it allows a multiresolution representation of G_0 by bounding its size. It allows a reasonable time step by quenching the high-frequency noise endemic in the multiresolution wavelet representation. The band-limit is controlled by the cut parameter ξ , which confines the Coulomb singularity removing the high-momentum components and their associated propagation error. Finally, the separated nature of G_0 allows robust scaling on distributed memory computers.

C. Model potential

Since our eventual objective is the treatment of general polyatomic systems without symmetry, we cannot rely on the Jacobian of special coordinates to exactly represent the Coulomb singularity in an integrable fashion. Thus we use a smoothed approximation successfully employed in Hartree-Fock and density functional computations [16] to model a nuclear potential of charge Z :

$$V_{\text{model}}(r) = \frac{\text{erf}(r)}{r} + \frac{e^{-r^2}}{\sqrt{\pi}}. \quad (16)$$

The coefficient of the Gaussian term is chosen so that the mean error is zero:

$$\int_0^\infty r^2 \left(V_{\text{model}}(r) - \frac{1}{r} \right) dr = 0. \quad (17)$$

The depth of the model potential [see Fig. 2(a)],

$$V_\xi(r) = \frac{Z}{\xi} V_{\text{model}}\left(\frac{r}{\xi}\right), \quad (18)$$

controls the maximum momentum component allowed in the wave function and is controlled by the cut parameter ξ . The band-limit $c = 5/\xi$ [shown in the inset of Fig. 2(b)] has been empirically determined. The coarsest potential ($\xi = 0.3$) agrees with the Coulomb function to machine precision when $r > 2$, and smaller ξ values produce an arbitrarily accurate agreement,

$$\lim_{\xi \rightarrow 0} V_\xi(r) = -\frac{Z}{r}. \quad (19)$$

Since rescattering is understood to be sensitive to the finest length scales [48], we emphasize the importance of the ξ convergence study in Sec. III B 3.

It is desirable to begin the simulation with a stationary state of V_ξ . The initial Coulomb eigenstate is relaxed into an eigenstate of the model potential through the following self-consistent solution:

$$\psi(\mathbf{r}) = \left(-\frac{1}{2}\nabla^2 - E \right)^{-1} V_\xi(r) \psi(\mathbf{r}). \quad (20)$$

III. OBSERVABLES AND CONVERGENCE

As a necessary prelude to applications in higher dimensional systems, we benchmark this method with 3D hydrogenic ions and establish its convergence.

A. Projection

The spatial representation and time propagation are directly generalized to 3D. Projection onto the bound and scattering states, however, is unique to the geometry of each system. Analytic eigenfunctions make the hydrogenic systems a natural test case.

1. Transition amplitudes

The ionization spectrum is calculated by projecting the wave function onto the incoming spherical wave

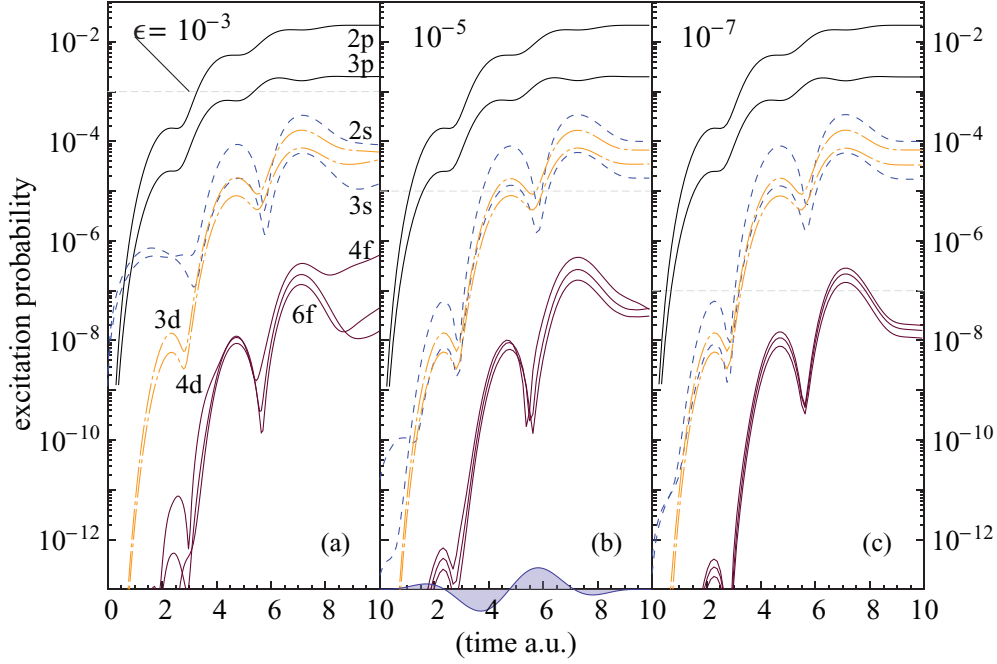


FIG. 4. (Color online) The bound state probabilities of He^+ as calculated in Eq. (22) for different values of the numerical truncation threshold ϵ (a) 10^{-3} , (b) 10^{-5} , and (c) 10^{-7} . ϵ is represented by the horizontal dashed line. See labels in (a) for legend.

eigenstates [49] of the field-free Coulomb potential:

$$\phi_{\mathbf{k}}^{(-)}(\mathbf{r}) = (2\pi)^{-3/2} e^{\pi\eta/2} \Gamma(1+i\eta) e^{i\mathbf{k}\cdot\mathbf{r}} \times {}_1F_1(-i\eta, 1, -ikr - i\mathbf{k}\cdot\mathbf{r}) \quad (21)$$

for nuclear charge Z , momentum of magnitude k , and $\eta = Z/k$. These Coulomb scattering states are momentum normalized, $\langle \phi_{\mathbf{k}'}^{(-)} | \phi_{\mathbf{k}}^{(-)} \rangle = \delta^3(\mathbf{k}' - \mathbf{k})$.

The softening of the Coulomb singularity in Eq. (20) implies the Coulomb eigenstates are not eigenfunctions of the new model potential and have a nonzero overlap with the initial state. Since the eigenstates of V_ξ are too expensive to compute directly, we remove the nonphysical overlap between the Coulomb eigenfunctions and those of the initial state of the model potential:

$$P_{n\ell} = |\langle \phi_{n\ell} | \psi(T) \rangle - \langle \phi_{n\ell} | \psi(0) \rangle \langle \psi(0) | \psi(T) \rangle|^2, \quad (22)$$

$$\Upsilon_{\mathbf{k}} = |\langle \phi_{\mathbf{k}} | \psi(T) \rangle - \langle \phi_{\mathbf{k}} | \psi(0) \rangle \langle \psi(0) | \psi(T) \rangle|^2. \quad (23)$$

Equations (22) and (23) describe this first-order Gram-Schmidt correction to the transition amplitudes. The second-order error is visible in the initial value ($t = 0$) of the transition probability to the spherically symmetric s states P_{ns} and can be seen about 5 orders of magnitude below ϵ in Fig. 4.

The partial integration of Eq. (23) provides the single differential probability distributions,

$$\begin{aligned} \frac{dP}{dE_f} &= \int |\Upsilon_{\mathbf{k}}|^2 k d\Omega_k, & \frac{dP}{d\Omega} &= \int |\Upsilon_{\mathbf{k}}|^2 k^2 dk, \\ \frac{dP}{dk} &= \int |\Upsilon_{\mathbf{k}}|^2 k^2 d\Omega_k, \end{aligned} \quad (24)$$

where E_f is the kinetic energy of the freed electron.

2. Angular projection

To determine the relative strength of each ionization process in Table III we computed the difference between the total angular-momentum-resolved probability coefficients $|c_\ell|^2$ and those of the individual bound states. The partial wave expansion

$$\psi(r, \theta) = \sum_{\ell} C_{\ell}(r) Y_{\ell 0}(\theta) \quad (25)$$

provides the ℓ th radial distribution

$$C_{\ell}(r) = \langle Y_{\ell 0} | \psi \rangle_{\Omega}, \quad (26)$$

projecting the wave function onto the ℓ th spherical harmonic by integrating over concentric spherical shells. Since ψ is normalized, the total angular probability can be found by integrating $C_{\ell}(r)$:

$$|c_{\ell}|^2 = \int |C_{\ell}(r)|^2 r^2 dr. \quad (27)$$

The angular component of ionization

$$|c_{\ell}^{\text{ion}}|^2 = |c_{\ell}|^2 - \sum_n |\langle \phi_{n\ell} | \psi \rangle|^2 \quad (28)$$

is simply the difference between the total and bound probability of the ℓ th component.

B. Convergence

In this section we study the effects of the sources of error in our numerical scheme: the numerical truncation threshold ϵ , the size of the time step dt , and the model potential cutoff parameter ξ . ϵ sets an upper bound on local error, and the time propagation error is proportional to the size and number of time steps. The cutoff parameter ξ determines the highest

frequency allowed in the wave function by controlling the depth of the model potential and the band-limit of the free-particle propagator.

1. Truncation error

MADNESS's adaptive refinement allows arbitrary accuracy. However, finite resources impose a limit on the spatial refinement. This is realized by the truncation threshold ϵ which controls the local error. While the error in the wave function accumulates over multiple time steps, potentially becoming greater than ϵ , some transition amplitudes achieve convergence below ϵ .

To determine the effect of ϵ on the system, we present the dynamics of the transition probabilities in Fig. 4 computed at three different truncation thresholds $\epsilon = 10^{-3}, 10^{-5}$, and 10^{-7} . Visually, the dynamics of the $2s$, $3d$, and p states are converged with $\epsilon = 10^{-3}$, whereas the $3s$ and $4d$ states require $\epsilon = 10^{-5}$ for convergence. Numerical error is also readily apparent for states with populations that continue to evolve after the end of the pulse. In contrast to the insufficiently converged f states [Figs. 4(a) and 4(b)] one can observe the parallel curves within a converged angular momentum group. Nevertheless, these unconverged states are within an order of magnitude of their final value in Fig. 4(c).

Figure 5 shows the response of the photoionization momentum spectrum to ϵ . While the ionization of hydrogen is unaffected by ϵ , the weak ionization processes in He^+ [Fig. 5(b)] are more sensitive and thus misrepresented when $\epsilon > 10^{-6}$.

Table I shows convergence trends in the transition probabilities of He^+ . The one-photon transition probabilities to the $2p$ state is correct to three digits for $\epsilon = 10^{-3}$, and the two-photon transitions to the s and d states have errors on the order of 10%. An unconverged state changes with successively smaller ϵ (see 5g), while a converged state oscillates about the correct value (see $2p$ and $2s$).

2. Time step error

At each time step dt , error is accumulated from the size of the time step ϵ_{dt} and the truncation ϵ_{trunc} of the adaptive basis,

$$\epsilon_{\text{total}} = O\left(\frac{T\epsilon_{\text{trunc}}}{dt}\right) + O\left(\frac{T\epsilon_{dt}}{dt}\right). \quad (29)$$

For large time steps ϵ_{dt} dominates, whereas small dt implies many time steps and hence greater overall truncation error. Figure 6(a) shows how different time steps affect the energy (expectation of the Hamiltonian) of hydrogen. At the end of the pulse, the relative error of Fig. 6(a) is shown in Fig. 6(b). For $dt/t_{\text{crit}} = 10$ we see a slight deviation in the energy which quickly diverges for larger values as ϵ_{dt} dominates. The photoionization peak in Fig. 6(c) is largely insensitive to dt . However, the peak of the smallest time step is slightly shifted to the right as ϵ_{trunc} accumulates after many time steps. Thus, the high-order symplectic integrator [45] is beneficial in enabling large time steps. The illustrations presented in Sec. IV use $dt = 5t_{\text{crit}}$.

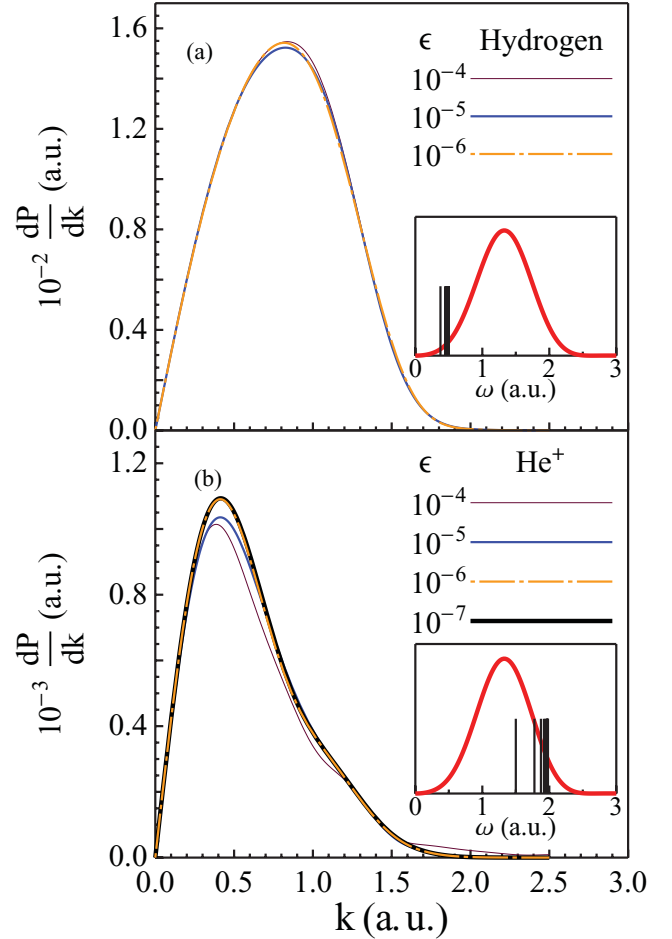


FIG. 5. (Color online) The photoionization momentum spectra for different values of the numerical threshold ϵ for (a) H ($\xi = 0.1$) and (b) He^+ ($\xi = 0.06$).

3. The cutoff parameter

The length scale on which the model potential is smoothed can be thought of as the closest scattering distance or cutoff parameter (ξ). In this section we probe the aberrations caused by its modification.

Figure 7(a) shows the dynamic energy $\langle \hat{H} \rangle$ [where \hat{H} is the Hamiltonian from Eq. (1)] of hydrogen for different ξ . Smaller ξ lead to a lower, more accurate ground-state energy E_0 which converges toward the analytic value of -0.5 in Fig. 7(d). The relative position of the transition energies in atomic hydrogen and the power spectrum of the laser [see the inset in Fig. 5(a)] predict single-photon ionization as the dominant process. As $\xi \rightarrow 0$, higher energy events are included and the change in energy of the system

$$\Delta E = E(T) - E_0 \quad (30)$$

increases as $\xi \rightarrow 0$ [see Fig. 7(e)]. This can also be seen for the total inelastic excitation

$$P(t) = 1 - |\langle \psi(0) | \psi(t) \rangle|^2 \quad (31)$$

[Fig. 7(h)] and total ionization [Fig. 8(a)].

While the convergence of hydrogen depends on high-energy events, the convergence of He^+ is related to the stability of the ground state. In He^+ the ΔE [Fig. 7(g)], the total inelastic

TABLE I. Convergence of the transition probabilities of He^+ with $L \in [-1000, 1000]$. $\xi = 0.059$ for the study (top), and $\epsilon = 10^{-7}$ during convergence of ξ . The bound states were summed up to $n = 9$.

ϵ	1s	2s	2p	3d	4f	5g	ΣP_{bound}	P_{ion}
10^{-3}	0.974448	0.851×10^{-4}	0.021424	6.03×10^{-5}	5.6×10^{-7}	7×10^{-7}	0.999016	8.58×10^{-4}
10^{-4}	0.974507	1.059×10^{-4}	0.021432	6.52×10^{-5}	2.7×10^{-6}	2×10^{-7}	0.999108	8.01×10^{-4}
10^{-5}	0.974513	0.998×10^{-4}	0.021415	6.67×10^{-5}	4.2×10^{-8}	1×10^{-9}	0.999081	8.28×10^{-4}
10^{-6}	0.974512	0.999×10^{-4}	0.021422	6.72×10^{-5}	2.1×10^{-8}	2×10^{-10}	0.999060	8.43×10^{-4}
10^{-7}	0.974516	0.996×10^{-4}	0.021409	6.70×10^{-5}	2.0×10^{-8}	1×10^{-11}	0.999057	8.49×10^{-4}
ξ								
0.2	0.97678	1.158×10^{-4}	0.02520	6.96×10^{-5}	1.4×10^{-7}	7×10^{-8}	0.99890	8.97×10^{-4}
0.12	0.97319	1.017×10^{-4}	0.02244	6.80×10^{-5}	2.2×10^{-8}	6×10^{-12}	0.99898	9.21×10^{-4}
0.08	0.97421	1.004×10^{-4}	0.02166	6.74×10^{-5}	2.6×10^{-8}	3×10^{-11}	0.99905	8.59×10^{-4}
0.06	0.97452	0.996×10^{-4}	0.02141	6.70×10^{-5}	2.0×10^{-8}	1×10^{-11}	0.99906	8.49×10^{-4}
0.05	0.97460	0.997×10^{-4}	0.02135	6.71×10^{-5}	2.2×10^{-8}	6×10^{-12}	0.99909	8.38×10^{-4}

state excitation [Fig. 7(i)], and the photoionization [Fig. 8(b)] decrease as the transition energies shift toward a less intense region of the power spectrum as $\xi \rightarrow 0$. See Table I for a quantitative comparison.

In the interest of gauging the accuracy of our calculations we generate a series of values with successively smaller ξ , interpolate between the lines, and mark the spot where the given quantity is within 1% of the final value [see the vertical dotted lines in Figs. 7(d)–7(i)]. The analytic value of the ground-state energy offers unambiguous convergence, for hydrogen $\xi_{1\%} \approx 0.24$ [Fig. 7(d)] and for He^+ $\xi_{1\%} \approx 0.08$. Systems with a larger nuclear charge (Z) require a smaller ξ for the same accuracy. In previous work [16] the value of ξ required to obtain a fixed accuracy for the total energy

was found to depend upon the atomic number Z according to $\xi \propto Z^{-5/3}$.

The effects of the smoothing can be seen in the oscillation of the z dipole (Fig. 9). As ξ decreases from $0.2 \rightarrow 0.059$, larger transition energies have two effects. First, the dipole amplitude is damped: $|c_{2p}^{(0.059)}|^2 < |c_{2p}^{(0.2)}|^2$ (see Table I). Second, the period of oscillation increases. While $t \in (10, 50)$, the dipole moment of $\xi = 0.2$ oscillates 9 times, while that of $\xi = 0.059$ oscillates 9.5 times. This yields a $1s \rightarrow 2p$ transition energy of $\omega_{12} = 2\pi/T = 1.496$, which deviates 0.2% from the analytic value of 1.5. The broadband laser pulse also excites the $3p$ state, whose presence can be seen by the beats of the modulating envelope with a period only 13% away from the predicted value of $5/36$: $\omega_{23} = 2\pi/T = 2\pi/(38 - 12) = 0.242$.

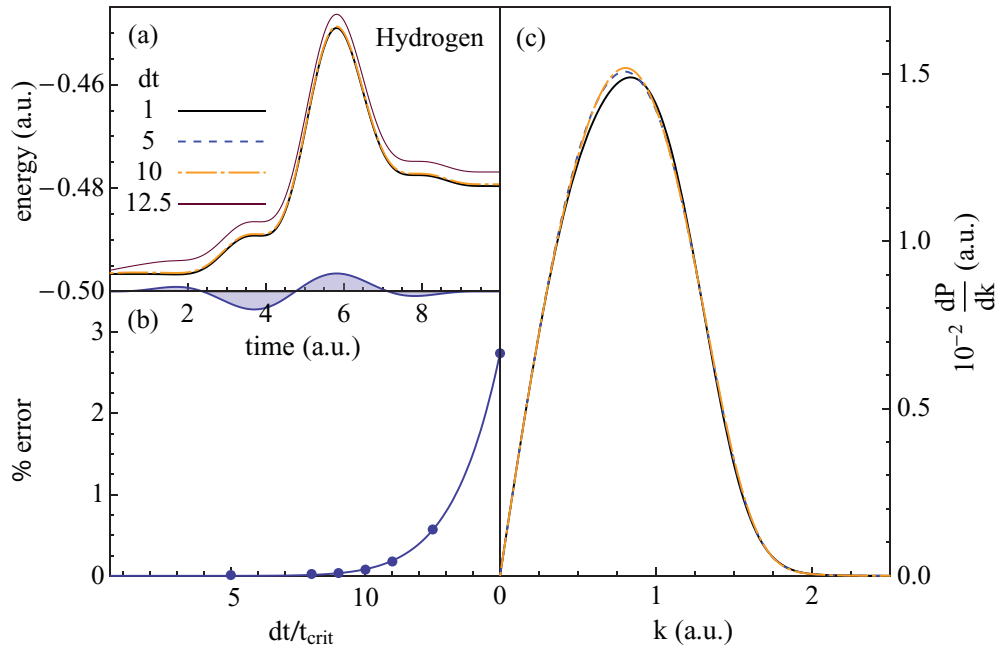


FIG. 6. (Color online) The dynamic convergence of atomic hydrogen ($\xi = 0.2$, $\epsilon = 1 \times 10^{-5}$, and $dt_{\text{crit}} = 3.4 \times 10^{-3}$) with respect to the time step dt . The energy (\hat{H}) from Eq. (1) is shown in (a) along with its error, at different time steps, at the end of the pulse in (b). (c) The photoionization spectrum [see Eq. (24)].

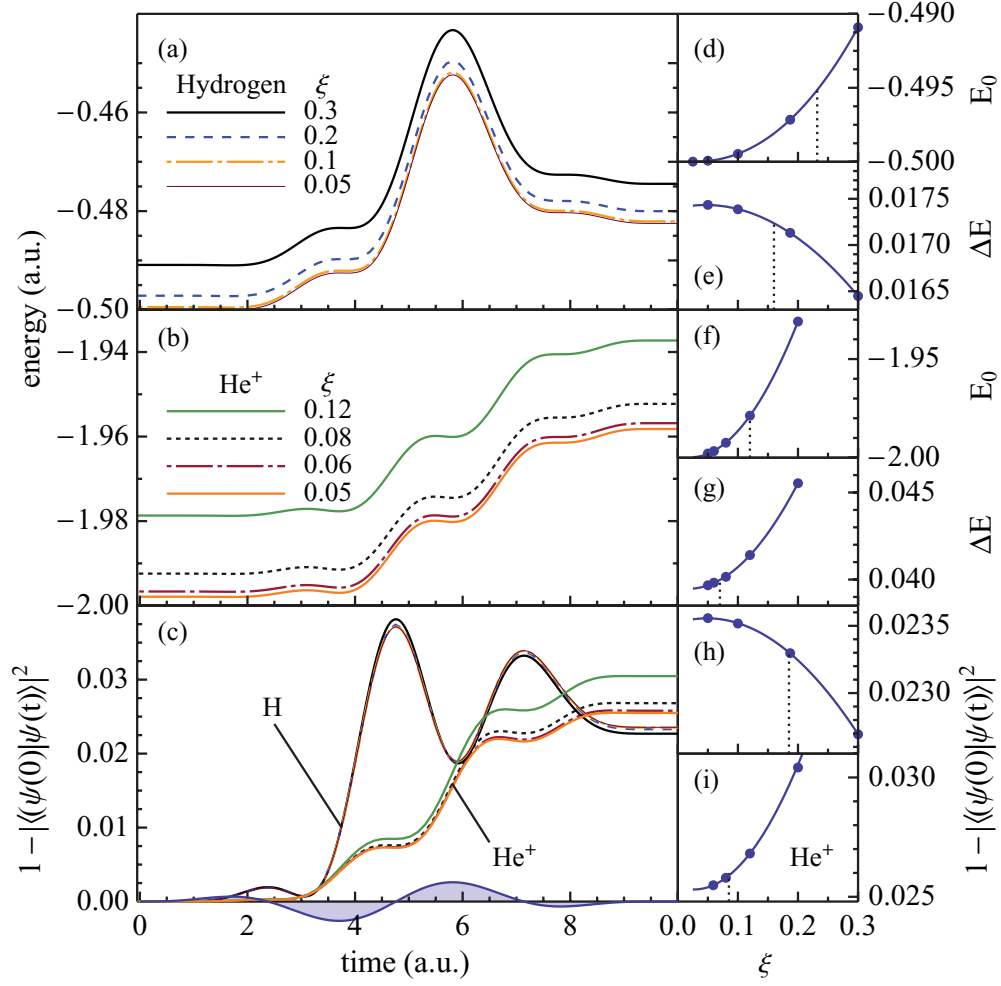


FIG. 7. (Color online) The dynamic convergence of H and He^+ with respect to the cut parameter ξ is shown for the energy $\langle \hat{H} \rangle$ from Eq. (1) in (a) & (b) and the total inelastic excitation vs time from Eq. (31) in (c). Convergence of the ground-state energy (d) & (f), the energy difference from Eq. (30) in (e) & (g), and total inelastic excitation in (h) & (i) are shown as a function of ξ . The dotted line represents convergence within 1% of the extrapolated value.

4. Box size, norm, and timing issues

The simulation box is a cube $[-L, L]^3$ deliberately chosen to be much larger than the final wave packet to avoid reflection or the need for absorbing boundary conditions. In MADNESS, the size of the *sparse* wave function ψ scales as $O(\log(L))$. The *dense* momentum eigenfunctions $\phi_{\mathbf{k}}^{(-)}(\mathbf{r})$, however, fill the entire simulation box scaling as $O(L^3)$. For efficiency we compute $\phi_{\mathbf{k}}^{(-)}(\mathbf{r})$ in a reduced volume corresponding to the furthest extent,

$$L_{\text{small}} = T\sqrt{2(n\omega - I_p)}, \quad (32)$$

of an n -photon ionization from the beginning of the pulse to escape from an ionization potential I_p . A two- and five-photon ionization of hydrogen corresponds to $L_{\text{small}} = 19$ and 35 in the current pulse. The largest relative truncation error in the ionization probability $k^2 \Upsilon_{\mathbf{k}}$ is on the order of 10^{-5} . L_{small} will be a more important issue, with infrared pulses in the tunneling regime where the electron is carried much further from the atom.

The loss of norm

$$\varepsilon_{\text{norm}}(t) = |1 - \langle \psi(t) | \psi(t) \rangle| \quad (33)$$

is due to several factors: the finite precision of the spatial representation of the wave function, and the repeated application of the band-limited propagator. While the split-operator time evolution schemes preserve norm and are unitary, norm is lost through the truncation of the high-frequency coefficients. Typically this loss accumulates uniformly throughout the pulse, ending with $\varepsilon_{\text{norm}}$ approximately 10ϵ . Occasionally $\varepsilon_{\text{norm}}(T) < \epsilon$, while the worst deviation (atomic hydrogen with $\epsilon = 10^{-7}$, $\xi = 0.1$) had $\varepsilon_{\text{norm}}(T) \approx 100\epsilon$.

The application cost of G_0 , which is related to its spatial extent and the size of the wave function, is affected by several interrelated parameters. First, the size of G_0 and the wave function is affected by ϵ . Second, the cost is directly proportional to the number of time steps:

$$N_t = T/dt \propto T/\xi^2. \quad (34)$$

While dt and ξ directly affect N_t , they also add to the complexity of G_0 . The electron propagates further during

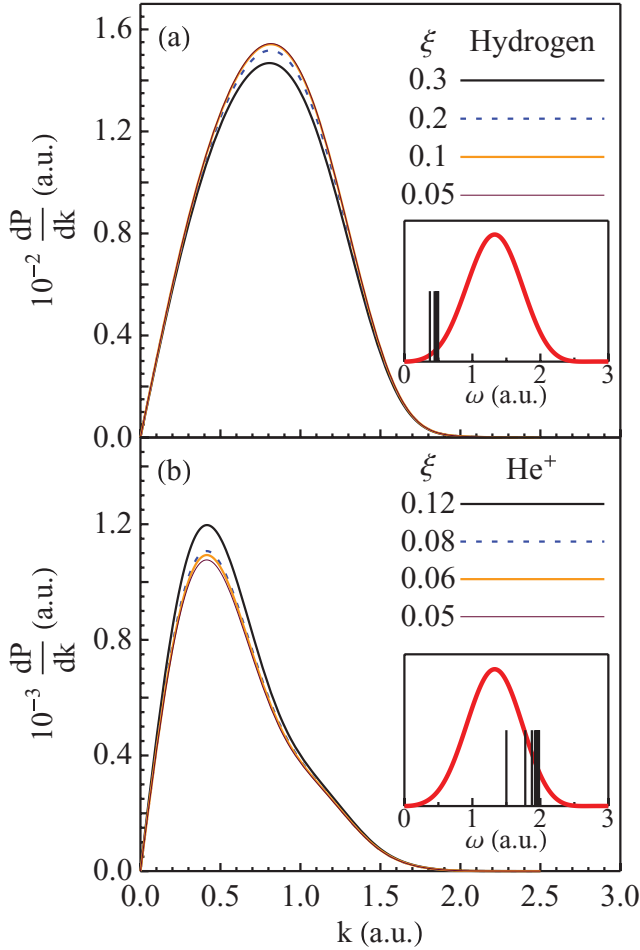


FIG. 8. (Color online) Convergence of the photoionization momentum distribution ($\epsilon = 10^{-7}$) with respect to ξ for (a) H and (b) He^+ . The relationship between the energy levels and the laser power spectrum is shown in the insets.

longer time steps; this increases the spatial extent of G_0 (L_{prop}). Smaller ξ increases the band-limit c and includes larger momentum components $|\mathbf{k}_{\text{max}}|$, which enlarges L_{prop} :

$$L_{\text{prop}} \propto \xi^{-1} \propto c \propto |\mathbf{k}_{\text{max}}|. \quad (35)$$

On an eight-core Intel Xeon 2.9-GHz computer with 24 GB of shared memory, the time evolution of H in 3D ($L = 300, k = 12, \epsilon = 10^{-5}, dt = 5dt_{\text{crit}}, \xi = 0.2$) was accomplished in about an hour. Higher accuracy requires more memory, which becomes the limiting factor on larger calculations. For He^+ ($L = 300, k = 24, \epsilon = 10^{-7}, dt = 4dt_{\text{crit}}, \xi = 0.059$) a typical high-fidelity time evolution took 46 hours running on a Cray XT5 running with 2000–5000 cores. Both time evolution and projection code realize performance increase (for sufficiently complex wave functions) through 12 000 cores.

C. Comparison to Prior Work

Pronin *et al.* [50] used perturbation theory to find the ionization of atomic hydrogen in a two-cycle pulse of the same frequency and intensity. However, their velocity gauge scheme applied the \sin^2 pulse envelope to the vector potential

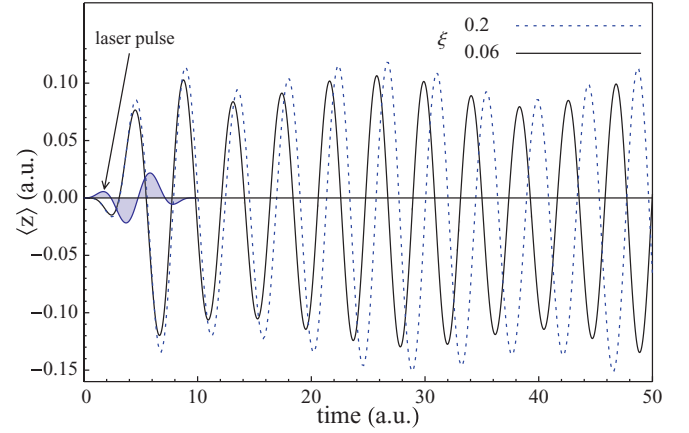


FIG. 9. (Color online) The dipole moment $\langle z \rangle$ for He^+ as a function of time for $\xi = 0.2$ and 0.059 . The period changes with ξ , illustrating the shift in the bound-state energies.

rather than the electric field, yielding a qualitatively different photoionization spectrum. Grum-Grzhimailo *et al.* [13] noted this and ran a series of computations with a four-cycle laser pulse at peak intensity $1.0 \times 10^{15} \text{ W/cm}^2$ ($E_0 = 0.169$) and central frequency $\omega = 0.3$ (152 nm), testing the effect of the pulse envelope on the vector potential and electric field on the photoionization spectrum of atomic hydrogen. We reproduced the photoionization spectrum in Fig. 10 for comparison purposes and obtained excellent agreement.

IV. ILLUSTRATIVE EXAMPLES

We present the highlights of our method with H, He^+ , Li^{2+} , and H_2^+ subject to the attosecond laser pulse [43] described in Fig. 1. This intense, two-cycle pulse with $I = 1 \times$

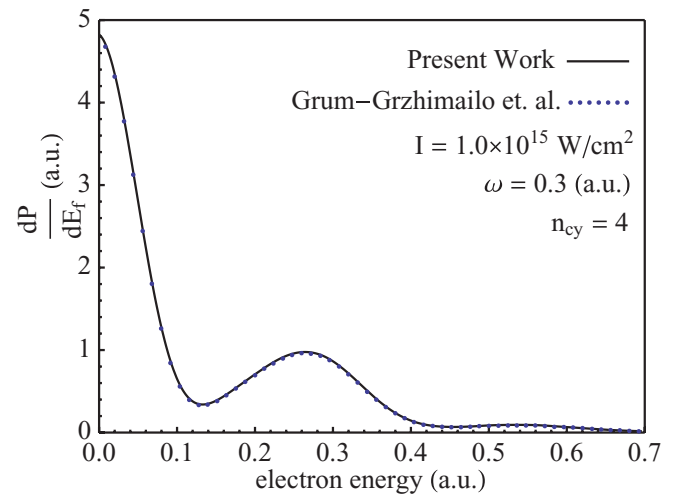


FIG. 10. (Color online) The photoionization spectrum of the present work is compared with that of Grum-Grzhimailo *et al.* [13] for atomic hydrogen in a four-cycle laser pulse with a \sin^2 envelope applied to the electric field, having a peak intensity of $1.0 \times 10^{15} \text{ W/cm}^2$ ($E_0 = 0.169$) and a central frequency of $\omega = 0.3$ (152 nm).

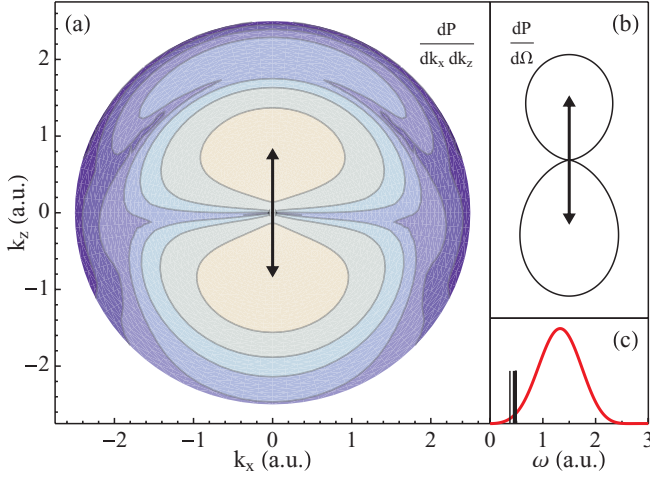


FIG. 11. (Color online) (a) The full differential photoionization momentum distribution of atomic hydrogen and (b) angular distribution $dP/d\Omega$ from Eq. (24) are shown against the laser polarization access (the arrow). (c) The transition energies in hydrogen are superimposed on the power spectrum of the laser.

10^{15} W/cm^2 ($E_0 = 0.176$) and driving frequency $\omega = 1.32$ yields a Keldysh parameter

$$\gamma = \frac{\omega}{E} \sqrt{2I_p} \quad (36)$$

of $\gamma = 8, 15$, and 11 for the ionization potential $I_p = 0.5, 2.0$, and 1.125 of H , He^+ , and Li^{2+} respectively, which is in the multiphoton regime ($\gamma > 1$). Access to the wave function enables us to calculate the transition probabilities, photoionization spectrum, and dynamic observables such as the energy and dipole moments.

A. Atomic hydrogen

Single-photon ionization dominates atomic hydrogen ($\epsilon = 10^{-7}$, $\xi = 0.05$, and $L = 3000$), as suggested by the relative position of the laser pulse power spectrum and the transition energies in Fig. 11(c). Figure 11(b) shows the signature dipole radiation pattern in the single differential cross section [from Eq. (24)], where the arrow represents the laser polarization axis. The logarithmic contour plot of the double photoelectron differential momentum distribution [Fig. 11(a)] shows a ridge of two-photon ionization just below the predicted value at $k = \sqrt{2(\omega - I_p)} = 2.1$, which is 3 orders of magnitude weaker than the dominant single photoionization process ionization. Table II shows quantitative results for selected transition probabilities.

TABLE II. Transition probabilities for atomic hydrogen, He^+ and Li^{2+} .

	1s	2s	2p	3d	4f	5g	ΣP_{bound}	P_{ion}
H	0.976	2.09×10^{-5}	5.03×10^{-3}	1.17×10^{-6}	2.4×10^{-7}	10^{-13}	0.0076	0.016
He^+	0.975	1.00×10^{-4}	2.14×10^{-2}	6.72×10^{-5}	2.1×10^{-8}	10^{-12}	0.025	8.5×10^{-4}
Li^{2+}	2.8×10^{-6}	0.965	1.1×10^{-6}	2.55×10^{-6}	1.3×10^{-8}	—	0.023	0.010

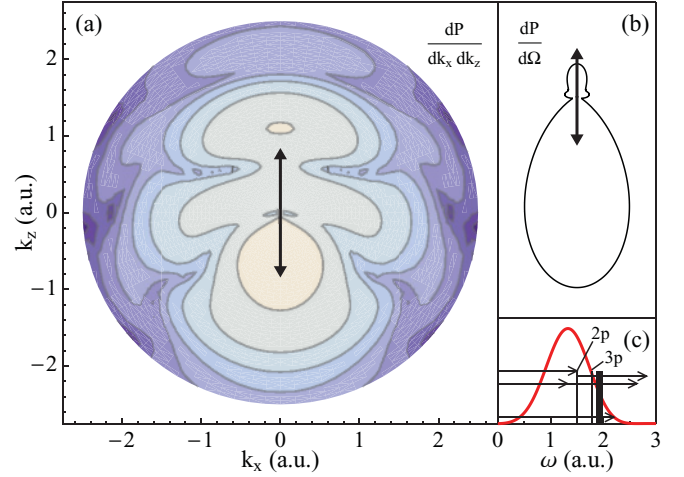


FIG. 12. (Color online) (a) The fully differential photoionization momentum distribution of Li^{2+} and (b) angular distribution $dP/d\Omega$ from Eq. (24) are shown against the laser polarization access (the arrow). (c) The transition energies from the ground state are superimposed on the power spectrum of the laser.

B. He^+

He^+ ($\epsilon = 10^{-7}$, $\xi = 0.05$, and $L = 1000$) is best explored in contrast to hydrogen, where excitation rather than ionization is the dominant process since the $1s \rightarrow 2p$ transition lies near the peak of the power spectrum [see Fig. 11(c)]. The dynamic behavior of the total inelastic excitation in Fig. 7(c) exemplifies this difference. In He^+ , the resonantly pumped electron has monotonically increasing excitation. The excitation of the loosely bound electron in hydrogen oscillates as it is driven back and forth across the origin. The dynamics of the total energy $\langle \hat{H} \rangle$ in Figs. 7(a) and 7(b) show similar behavior.

The weaker photoionization of He^+ in Fig. 12(a) has competition among ionization mechanisms [see arrows in Fig. 12(c)]. The single-photon ionization relies on a weak component of the power spectrum, while two- and three-photon, nonsequential ionization has peaks at $k = 1.1$ and 2.0 , respectively. Sequential double ionization occurs (primarily) through the $2p$ and peaks at 1.28 . We differentiate these processes by analyzing the coefficients of the partial wave expansion [see Eq. (28) in Sec. III A 2]. $|c_p|^2$ and $|c_d|^2$ comprise 98% of the ionization probability, with a small fraction coming from the s and f states (see Table III).

C. Li^{2+}

The $1s$ ground state of Li^{2+} ($\xi = 0.03$, $\epsilon = 10^{-6}$, and $L = 1000$) lies 3.375 units of energy below the excitation to the $2p$ state and 4.5 units below the continuum edge, requiring multiple photons from our laser pulse. The resulting transition

TABLE III. The angular resolved ionization coefficients for He+.

ℓ	$ c_{\ell}^{\text{ion}} ^2$
0	1.39×10^{-5}
1	5.20×10^{-4}
2	3.56×10^{-4}
3	3.88×10^{-6}

probabilities are almost all below the numerical threshold ϵ . The metastable $2s$ state of Li^{2+} , however, yields more interesting results.

Figure 13 shows the bound-state population dynamics of $\text{Li}^{2+}(2s)$. Ionization and dipole excitation to the $3p$ state are the leading events with similar probability. The $2s \rightarrow 1s$ channel has no single-photon transitions; consequently the $1s$ population does not follow the field, as do the other states, but increases to saturation in the middle of the pulse. The $2s \rightarrow 2p$ transition is significantly smaller than the other p transitions, since the power spectrum of the laser pulse has no dc component ($\omega = 0$) for transition between the degenerate states [see Fig. 14(c)]. Its most probable three-photon pathway are $2s \rightarrow 4p \rightarrow 3d/3s \rightarrow 2p$. The three forward peaks in the photoionization spectrum of Li^{2+} in Fig. 14(a) ($k = 0.6, 1.7$, and 2.4) correspond to the one-, two-, and three-photon ionization ($\omega = 1.32$).

D. H_2^+

The computational flexibility of MADNESS's Cartesian coordinates is best exemplified in H_2^+ . No new code was needed to run the molecular system, only a modification of the input file. The internuclear degree of freedom was included by using a 4D wave function and adding a nuclear-nuclear term to the Hamiltonian.

The mass of the fourth coordinate s was scaled to unity

$$s = \sqrt{\mu} R, \quad s \in [0, \sqrt{\mu} R_{\text{max}}], \quad \mathbf{r} = (x, y, z, s), \quad (37)$$

where μ is the reduced mass of the two protons and R is the internuclear coordinate. This allows a uniform application

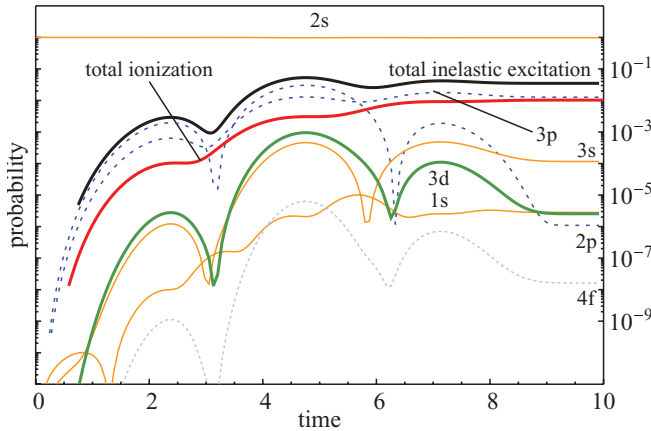


FIG. 13. (Color online) The total ionization and inelastic excitation probability [see Eq. (31)] of Li^{2+} and bound-state transition probabilities $|\langle \psi_{n\ell 0} | \psi(t) \rangle|^2$ are plotted versus time.

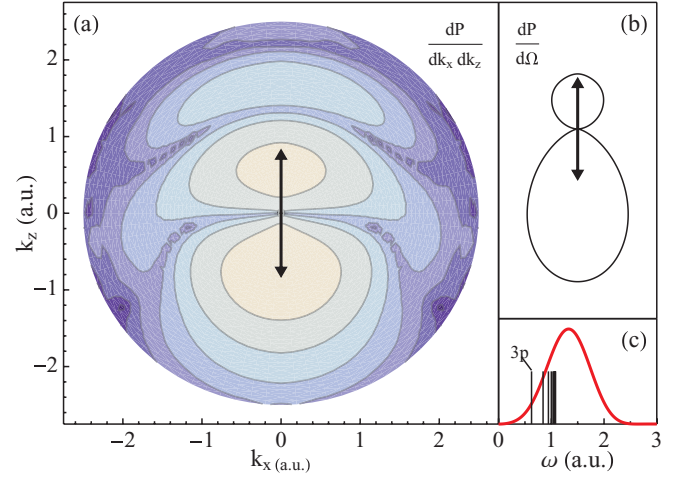


FIG. 14. (Color online) (a) The fully differential photoionization momentum distribution of Li^{2+} and (b) angular distribution $dP/d\Omega$ from Eq. (24) are shown against the laser polarization access (the arrow). (c) The transition energies from the initial $2s$ state are superimposed on the power spectrum of the laser.

of the free-particle propagator. The initial internuclear wave function was approximated by the ground state of the harmonic oscillator centered at $R_0 = 2.0$:

$$\begin{aligned} \psi(R) &= \left(\frac{\mu \omega}{\pi} \right)^{\frac{1}{4}} e^{\mu \omega (R-R_0)^2/2}, \\ \psi(s) &= \left(\frac{\omega}{\pi} \right)^{\frac{1}{4}} e^{\omega(s-\sqrt{\mu}R_0)^2/2}. \end{aligned} \quad (38)$$

Finally, the fully coupled, 4D wave function was relaxed into the numerical ground state as described in Sec. II C.

Inclusion of the nuclear-nuclear potential (V_{NN}) as discussed in Sec. II C was straightforward:

$$\begin{aligned} \hat{H} &= -\frac{1}{2} \nabla^2 + V_{eN}(\mathbf{r}) + V_{NN}(s) + \mathbf{E}(t) \cdot \mathbf{r}, \\ V_{eN}(\mathbf{r}) &= V_{\xi} \left(\sqrt{\left(x - \frac{s}{2\sqrt{\mu}} \right)^2 + y^2 + z^2} \right) \\ &\quad + V_{\xi} \left(\sqrt{\left(x + \frac{s}{2\sqrt{\mu}} \right)^2 + y^2 + z^2} \right), \\ V_{NN}(s) &= \frac{\sqrt{\mu}}{s}. \end{aligned} \quad (39)$$

It took about an hour to run the 3D simulation of H_2^+ using the same computer and parameters as the atomic hydrogen case mentioned in Sec. III B 4. The 4D H_2^+ ran on a few thousand cores of the XT5 Cray at Oak Ridge National Laboratory, taking just under 5 h. Figure 15 compares the electronic energy (expectation value of the Hamiltonian) as a function of time. The agreement between the two simulations is expected since nuclear motion is negligible on the attosecond time scale. The application of an infrared pulse should show a breakdown in the fixed nuclear approximation. The 4D scheme used the second-order accurate Trotter propagator that, along with finite precision computation, caused the aberration in the energy at the end of the pulse.

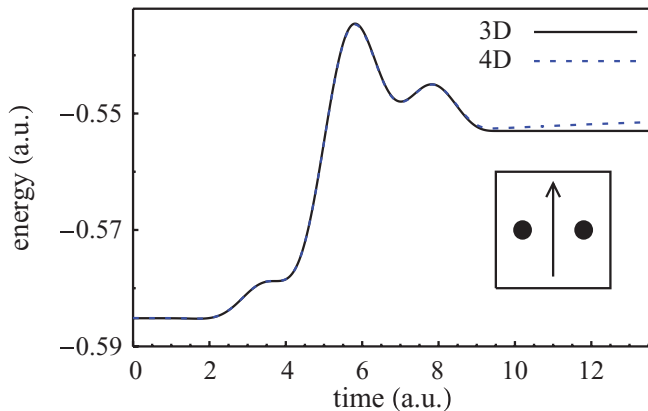


FIG. 15. (Color online) A comparison of the total energy of the 3D and 4D simulations of H_2^+ , with the internuclear axis oriented perpendicular to the laser field polarization axis, as shown by the inset.

V. CONCLUSIONS

We have introduced an explicit, *ab initio* scheme for solving the TDSE. Convergence was established for 3D hydrogenic systems in an attosecond pulse [43]. The accuracy was achieved with an adaptively refined mesh, large simulation box, and a high-order symplectic propagator. This scheme is readily extendible to higher dimensional systems, as shown by the 4D treatment of H_2^+ .

The direct photoionization of hydrogen was compared to that of He^+ , whose complex distribution came from the competition between ionization channels. Access to the

complete wave function allows dynamic access to observables. The energy and total inelastic excitation of resonant He^+ show a monotonic increase, while the same quantities in hydrogen oscillate as the loosely bound electron is driven back and forth with the field. The excitation dynamics of Li^{2+} allow the comparison of the dipole excitation $2s \rightarrow 3p$; the nonsequential, two-photon de-excitation $2s \rightarrow 1s$; and the three-photon sequential transition from $2s \rightarrow 2p$. Finally, a preliminary comparison of 3D and 4D calculations of H_2^+ was reported.

We have successfully implemented an explicit solution of the TDSE in the multiresolution framework for hydrogenic atoms and molecular systems in the multiphoton regime. Future work will examine high-harmonic generation and above-threshold ionization in the tunneling regime using the same numerical framework. These studies are, however, a precursor to high-dimensional, few-particle (electron and/or nuclei) wave functions and multiconfiguration self-consistent field calculations of many-electron systems.

ACKNOWLEDGMENTS

This work was supported by the NSF (N.V. and R.H.) under Grant OCI-0904972: Computational Chemistry and Physics Beyond the Petascale, by the office of Fusion Energy Sciences (P.K.), and the US Department of Energy at Oak Ridge National Laboratory. Simulations were performed at the National Center for Computational Sciences at Oak Ridge National Laboratory under Contract DE-AC05-00OR22725 from the Department of Energy.

- [1] K. C. Kulander, *Phys. Rev. A* **35**, 445 (1987).
- [2] X. Tong and S. Chu, *Chem. Phys.* **217**, 119 (1997).
- [3] T. Rescigno, M. Baertschy, W. Isaacs, and C. McCurdy, *Science* **286**, 2474 (1999).
- [4] J. Colgan, M. S. Pindzola, F. J. Robicheaux, D. C. Griffin, and M. Baertschy, *Phys. Rev. A* **65**, 042721 (2002).
- [5] V. D. Rodríguez, E. Cormier, and R. Gayet, *Phys. Rev. A* **69**, 053402 (2004).
- [6] A. Becker and F. Faisal, *J. Phys. B* **38**, R1 (2005).
- [7] L.-Y. Peng and A. F. Starace, *J. Chem. Phys.* **125**, 154311 (2006).
- [8] Z. Chen, T. Morishita, A.-T. Le, M. Wickenhauser, X. M. Tong, and C. D. Lin, *Phys. Rev. A* **74**, 053405 (2006).
- [9] M. G. Girju, K. Hristov, O. Kidun, and D. Bauer, *J. Phys. B* **40**, 4165 (2007).
- [10] S. Borbély, K. Tókei, and L. Nagy, *Phys. Rev. A* **77**, 033412 (2008).
- [11] L. A. A. Nikolopoulos, J. S. Parker, and K. T. Taylor, *Phys. Rev. A* **78**, 063420 (2008).
- [12] J. Madroñero and B. Piraux, *Phys. Rev. A* **80**, 033409 (2009).
- [13] A. N. Grum-Grzhimailo, B. Abeln, K. Bartschat, D. Weffen, and T. Urness, *Phys. Rev. A* **81**, 043408 (2010).
- [14] B. Alpert, G. Beylkin, D. Gines, and L. Vozovoi, *J. Comput. Phys.* **182**, 149 (2002).
- [15] T. Yanai, G. Fann, Z. Gan, R. Harrison, and G. Beylkin, *J. Chem. Phys.* **121**, 2866 (2004).
- [16] R. Harrison, G. Fann, T. Yanai, Z. Gan, and G. Beylkin, *J. Chem. Phys.* **121**, 11587 (2004).
- [17] G. Fann, G. Beylkin, R. Harrison, and K. Jordan, *IBM J. Res. Dev.* **48**, 161 (2004).
- [18] H. Wang, R. Acevedo, H. Mollé, J. L. Mackey, J. L. Kinsey, and B. R. Johnson, *J. Chem. Phys.* **121**, 7647 (2004).
- [19] D. K. Sparks and B. R. Johnson, *J. Chem. Phys.* **125**, 114104 (2006).
- [20] E. Lorin and A. D. Bandrauk, *Comput. Phys. Commun.* **181**, 626 (2010).
- [21] A. D. Bandrauk, S. Chelkowski, S. Kawai, and H. Lu, *Phys. Rev. Lett.* **101**, 153901 (2008).
- [22] I. Ben-Itzhak, P. Q. Wang, A. M. Sayler, K. D. Carnes, M. Leonard, B. D. Esry, A. S. Alnaser, B. Ulrich, X. M. Tong, I. V. Litvinyuk, C. M. Maharjan, P. Ranitovic, T. Osipov, S. Ghimire, Z. Chang, and C. L. Cocke, *Phys. Rev. A* **78**, 063419 (2008).
- [23] E. Kamarchik and D. A. Mazziotti, *Phys. Rev. A* **79**, 012502 (2009).
- [24] M. Nest, *Chem. Phys. Lett.* **472**, 171 (2009).
- [25] C. B. Madsen, M. Abu-samha, and L. B. Madsen, *Phys. Rev. A* **81**, 043413 (2010).
- [26] Y. H. Jiang, A. Rudenko, J. F. Pérez-Torres, O. Herrwerth, L. Foucar, M. Kurka, K. U. Kühnel, M. Toppin, E. Plésiat, F. Morales, F. Martín, M. Lezius, M. F. Kling, T. Jahnke,

- R. Dörner, J. L. Sanz-Vicario, J. van Tilborg, A. Belkacem, M. Schulz, K. Ueda, T. J. M. Zouros, S. Düsterer, R. Treusch, C. D. Schröter, R. Moshhammer, and J. Ullrich, *Phys. Rev. A* **81**, 051402(R) (2010).
- [27] D. J. Haxton, K. V. Lawler, and C. W. McCurdy, *Phys. Rev. A* **83**, 063416 (2011).
- [28] T. Bredtmann, S. Chelkowski, and A. D. Bandrauk, *Phys. Rev. A* **84**, 021401(R) (2011).
- [29] T. Gorczyca and N. Badnell, *J. Phys. B* **30**, 3897 (1997).
- [30] E. Smyth, J. Parker, and K. Taylor, *Comput. Phys. Commun.* **114**, 1 (1998).
- [31] T. Mercouris, C. Haritos, and C. A. Nicolaides, *J. Phys. B* **34**, 3789 (2001).
- [32] G. L. Kamta and A. F. Starace, *Phys. Rev. A* **65**, 053418 (2002).
- [33] I. Bray, *Phys. Rev. Lett.* **89**, 273201 (2002).
- [34] S. Laulan and H. Bachau, *Phys. Rev. A* **68**, 013409 (2003).
- [35] C. W. McCurdy, M. Baertschy, and T. N. Rescigno, *J. Phys. B* **37**, R137 (2004).
- [36] E. Fomouo, G. L. Kamta, G. Edah, and B. Piraux, *Phys. Rev. A* **74**, 063409 (2006).
- [37] M. S. Pindzola, F. Robicheaux, S. D. Loch, J. C. Berengut, T. Topcu, J. Colgan, M. Foster, D. C. Griffin, C. P. Ballance, D. R. Schultz, T. Minami, N. R. Badnell, M. C. Witthoef, D. R. Plante, D. M. Mitnik, J. A. Ludlow, and U. Kleiman, *J. Phys. B* **40**, R39 (2007).
- [38] I. A. Ivanov and A. S. Kheifets, *Phys. Rev. A* **75**, 033411 (2007).
- [39] A. Palacios, C. W. McCurdy, and T. N. Rescigno, *Phys. Rev. A* **76**, 043420 (2007).
- [40] L. A. A. Nikolopoulos and P. Lambropoulos, *J. Phys. B* **40**, 1347 (2007).
- [41] A. Palacios, D. A. Horner, T. N. Rescigno, and C. W. McCurdy, *J. Phys. B* **43**, 194003 (2010).
- [42] R. Pazourek, J. Feist, S. Nagele, E. Persson, B. I. Schneider, L. A. Collins, and J. Burgdörfer, *Phys. Rev. A* **83**, 053418 (2011).
- [43] G. Sansone, E. Benedetti, F. Calegari, C. Vozzi, L. Avaldi, R. Flammini, L. Poletto, P. Villoresi, C. Altucci, R. Velotta, S. Stagira, S. De Silvestri, and M. Nisoli, *Science* **314**, 443 (2006).
- [44] R. Harrison, [<http://code.google.com/p/m-a-d-n-e-s-s/downloads/list>], Implementation Notes (2011).
- [45] S. Chin and C. Chen, *J. Chem. Phys.* **114**, 7338 (2001).
- [46] D. J. Tannor, *Introduction to Quantum Mechanics: A Time-Dependent Perspective* (University Science Books, Hampshire, UK, 2007).
- [47] K. W. Morton and D. F. Mayers, *Numerical Solution of Partial Differential Equations* (Cambridge University Press, Cambridge, 2005).
- [48] A. Gordon, R. Santra, and F. X. Kärtner, *Phys. Rev. A* **72**, 063411 (2005).
- [49] L. D. Landau and E. M. Lifshitz, *Quantum Mechanics* (Butterworth, Heinemann, 1958), p. 570.
- [50] E. A. Pronin, A. F. Starace, M. V. Frolov, and N. L. Manakov, *Phys. Rev. A* **80**, 063403 (2009).